Draft version January 24, 2020
Typeset using LaTeX default style in AASTeX62

The Mega-MUSCLES Spectral Energy Distribution Of TRAPPIST-1

David J. Wilson,[1] Cynthia S. Froning,[1] Girish M. Duvvuri,[2] Kevin France,[2,3] Allison Youngblood,[4,3] P. Christian Schneider,[5] Zachory Berta-Thompson,[2] Alexander Brown,[2] Andrea P. Buccino,[6] Suzanne Hawley,[7] Jonathan Irwin,[8] Lisa Kaltenegger,[9] Adam Kowalski,[2,3,10] Jeffrey Linsky,[2] R. O. Parke Loyd,[11] Yamila Miguel,[12] J. Sebastian Pineda,[2] Seth Redfield,[13] Aki Roberge,[4] Sarah Rugheimer,[14] Feng Tian,[15] and Mariela Vieytes[16,16]

[1] *McDonald Observatory, University of Texas at Austin, Austin, TX 78712*
[2] *Department of Astrophysical and Planetary Sciences, University of Colorado, Boulder, CO 80309, USA*
[3] *Laboratory for Atmospheric and Space Physics, University of Colorado, 600 UCB, Boulder, CO 80309*
[4] *Goddard Space Flight Center, Greenbelt, MD 20771*
[5] *Hamburger Sternwarte, Gojenbergsweg 112, 21029 Hamburg*
[6] *Dpto. de Fsica, Facultad de Ciencias Exactas y Naturales (FCEN), Universidad de Buenos Aires (UBA), Buenos Aires, Argentina*
[7] *Astronomy Department, University of Washington, Seattle, WA 98195, USA*
[8] *Harvard-Smithsonian Center for Astrophysics, 60 Garden St., Cambridge, MA 02138, US*
[9] *Astronomy Department, Cornell University, Ithaca, NY 14853, USA*
[10] *National Solar Observatory, University of Colorado at Boulder, 3665 Discovery Drive, Boulder, CO 80303*
[11] *School of Earth and Space Exploration, Arizona State University, Tempe, AZ 85287*
[12] *Leiden Observatory, P.O. Box 9500, 2300 RA Leiden, The Netherlands*
[13] *Wesleyan University, Department of Astronomy and Van Vleck Observatory, 96 Foss Hill Dr., Middletown, CT 06459, USA*
[14] *University of Oxford, Clarendon Laboratory, AOPP, Sherrington Road, Oxford, OX1 3PU, UK*
[15] *State Key Laboratory of Lunar and Planetary Sciences, Macau University of Science and Technology, Macau, China*
[16] *Instituto de Astronoma y Fsica del Espacio (CONICET-UBA), Buenos Aires, Argentina.*

(Received Nov, 2019; Revised Nov, 2019; Accepted January 24, 2020)

Submitted to ApJ

ABSTRACT

We present a 5 Å–10 μm Spectral Energy Distribution (SED) of the ultracool dwarf star TRAPPIST-1, obtained as part of the Mega-MUSCLES Treasury Survey. The SED combines ultraviolet and blue-optical spectroscopy obtained with the *Hubble Space Telescope*, X-ray spectroscopy obtained with *XMM-Newton*, and models of the stellar photosphere, chromosphere, transition region and corona. A new Differential Emission Measure model of the unobserved extreme-ultraviolet spectrum is provided, improving on the Lyman α–EUV relations often used to estimate the 100–911 Å flux from low-mass stars. We describe the observations and models used, as well as the recipe for combining them into an SED. We also provide a semi-empirical, noise-free model of the stellar ultraviolet spectrum based on our observations for use in atmospheric modelling of the TRAPPIST-1 planets.

1. INTRODUCTION

Among the thousands of planetary systems that have been discovered over the past two and a half decades, TRAPPIST-1 is a standout case. Discovered by the TRansiting Planets and PlanestIsimals Small Telescope (TRAPPIST) survey in 2015 (Gillon et al. 2016), the system is comprised of an M8 ultracool dwarf star orbited by seven planets, all of which have similar masses and radii to Earth and Venus (Gillon et al. 2017; Wang et al. 2017). The planets are almost exactly coplanar, have orbital periods ranging between 1.5 and 18.8 days, and are all in an orbital resonance with at least one other planet (Luger et al. 2017). The system presents a challenging but achievable target for transit spectroscopy observations of the planets, both now with the *Hubble Space Telescope* (de Wit et al.

Corresponding author: David J. Wilson
djwilson394gmail.com

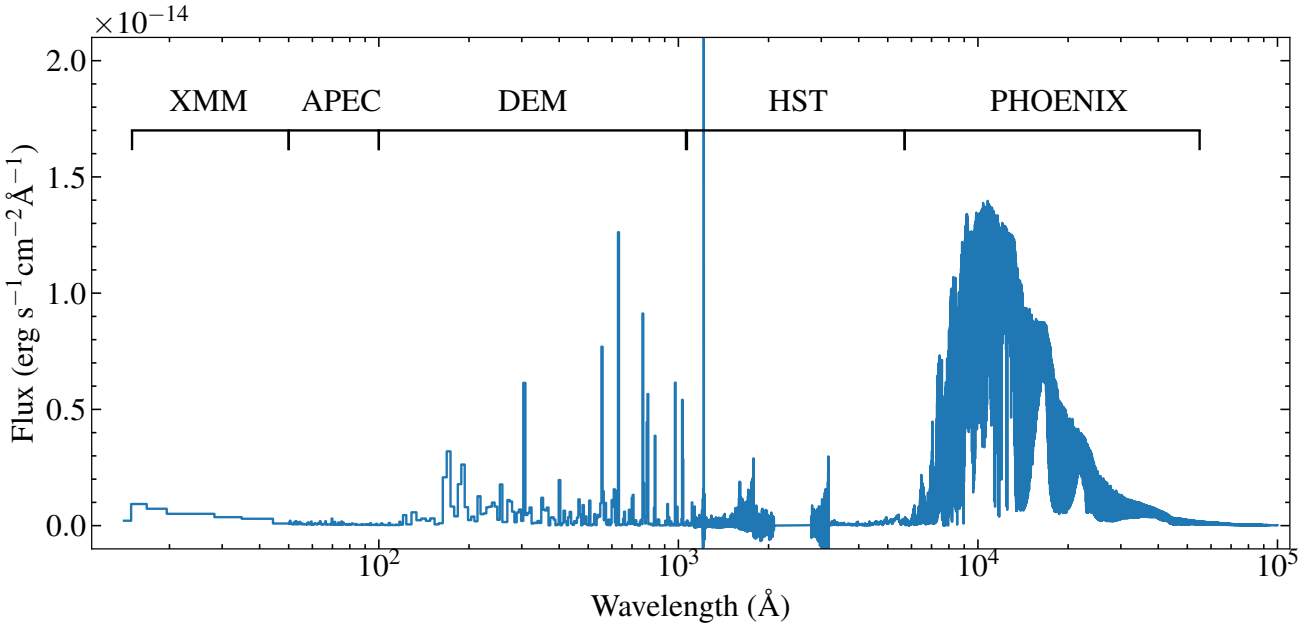

Figure 1. SED of TRAPPIST-1 with all data and models at native resolutions. The sources for each section of the spectrum are labeled above it.

2016) and in the future with the *James Webb Space Telescope* (Barstow & Irwin 2016; Morley et al. 2017). Three or four of the planets orbit at distances where the energy received from the star is such that liquid water might persist on their surfaces. The TRAPPIST-1 system therefore offers opportunities for comparative planetology to test models of planetary habitability, biosignatures and even, given the small orbital separations between the planets, transfer of material and/or life between the planets (Veras et al. 2018).

A complete evaluation of the potential habitability of the TRAPPIST-1 planets requires comprehensive knowledge of the parent star. This has proven challenging, with uncertainties remaining over, for example, the star's age (Burgasser & Mamajek 2017; Gonzales et al. 2019), activity (Vida et al. 2017), and rotation period (Roettenbacher & Kane 2017). Of particular importance, given the close proximity of the planets to the star, is the stellar magnetic activity and the resulting X-ray and ultraviolet emission. High-energy radiation can influence the retention and chemistry of planetary atmospheres as well as surface survival conditions (Rugheimer et al. 2015; Miguel et al. 2015; O'Malley-James & Kaltenegger 2017). However, TRAPPIST-1 is extremely faint at short wavelengths, making detailed characterisation of the high-energy environment in the system challenging. Wheatley et al. (2017) observed TRAPPIST-1 with *XMM-Newton* (*XMM*), finding variable X-ray luminosity with intensity similar to the modern quiescent Sun. Because of their proximity to the host stars, the planets would therefore experience XUV intensities much higher than the Earth, sufficient to significantly alter their atmospheres and strip away hydrogen from water in their atmospheres and (if present) oceans (Ribas et al. 2016; Airapetian et al. 2017). Bourrier et al. (2017a,b) obtained time series observations of the 1215.67Å Lyman α hydrogen emission line with *HST*, finding that it evolved over a three-month timescale but with no evidence for hydrogen (and thus water) escape from TRAPPIST-1c, which transited during their observations. Peacock et al. (2019) used the PHOENIX stellar atmosphere code to model the chromosphere and transition region of TRAPPIST-1, scaling it to the Bourrier et al. (2017a) Lyman α measurement and to distance-adjusted *GALEX* observations of stars with a similar spectral type. They found that the flux emitted between 100–912 Å varies by an order of magnitude depending on which calibrator was used. These studies demonstrate that accurately accounting for the effects of high-energy radiation on the TRAPPIST-1 planets requires spectroscopic observations at all accessible wavelengths.

Mega-MUSCLES (Measurements of the Ultraviolet Spectral Characteristics of Low-Mass Exoplanetary Systems) is an *HST* Treasury program obtaining 5 Å–10 μm spectral energy distributions (SEDs) of a representative sample of 13 M dwarfs, covering a wide range of stellar mass, age, and planetary system architecture and extending the original

11-star MUSCLES program (France et al. 2016; Youngblood et al. 2016; Loyd et al. 2016) to stars with lower masses, higher activity and/or faster rotation rates. Here we present the Mega-MUSCLES SED of TRAPPIST-1 (Figure 1), comprised of ultraviolet and X-ray spectroscopy with *HST* and *XMM*, along with state-of-the-art model spectra. We discuss the changes made to the data processing and stellar emission modelling implemented for Mega-MUSCLES compared with MUSCLES, present a semi-empirical model for use in model atmosphere simulations and compare the observed SED to the Peacock et al. (2019) models.

2. OBSERVATIONS

We observed TRAPPIST-1 with the Cosmic Origins Spectrograph (COS, Green et al. 2012) and the Space Telescope Imaging Spectrograph (STIS, Woodgate et al. 1998) onboard the *Hubble Space Telescope* (*HST*) on 2017 December 15, 2018 December 08–12 and 2019 June–08, for a total exposure time of 36379 s. The COS gratings used were G160M (8608 s), G130M (12404 s) and G230L (2731 s), and the STIS gratings were G430L (1795 s) and G140M (10841 s). Combined, these spectra cover the wavelength range 1130–5700 Å except for a gap between 2080–2790 Å which is not covered by the COS NUV detector and is too faint for STIS NUV observations. With the exception of the STIS/G430L exposure, the observations were obtained using photon-counting detectors in TIME-TAG mode. We extracted light curves from each spectrum to search for and potentially remove contributions from flares or other stellar activity, but found no significant variations.

For the COS G160M and G130M observations, variations in target position in the aperture between each orbit induce slight differences in wavelength calibration. To remove this effect we cross-correlated known emission lines in each x1d spectrum to shift each spectrum onto a single wavelength scale before coadding. Doing so provides a small increase in S/N and resolution compared with the x1dsum files produced by the CALCOS pipeline.

Four spectra were obtained with the STIS G140M grating, covering the Lyman α hydrogen line with a spectral range of 1195–1249 Å and R∼10000. The automated reduction pipeline failed to identify the spectral trace, so we used the flt images to visually identify the spectrum in each exposure, before re-extracting the spectrum with the STISTOOLS x1d routine, fixing the "a2center" keyword to the identified spectrum position. In one spectrum the trace could not be visually identified. Lyman α line fluxes in the spectra obtained immediately before and after the non-detection were similar, so the non-detection is unlikely to be due to intrinsic variability and probably an instrumental effect. The non-detection was therefore discarded, and the remaining three spectra coadded into the final G140M spectrum used hereafter.

TRAPPIST-1 has been observed multiple additional times with the STIS G140M grating both prior to and since our observations (Bourrier et al. 2017a,b). We initially intended to combine all of the available spectra, but we found the detected Lyman α flux to be variable, with the final coadded spectrum highly dependent on which subspectra were chosen for inclusion. Epoch-to-epoch changes are somewhat beyond the scope of this paper and we do not wish to preempt the teams leading the ongoing G140M observations, so we decided to use only the data obtained as part of the Mega-MUSCLES program. This has the advantage of ensuring that all of the data in the SED is contemporaneous, at the cost of improved S/N for the Lyman α measurement. We will reevaluate this decision when a full analysis of the G140M data is available and update the Mega-MUSCLES High-Level Science Products accordingly.

We further observed TRAPPIST-1 with *XMM-Newton* (*XMM*) using the EPIC instrument with thin filters for 23 ks on 2018 December 10, overlapping in time with the COS G130M observations. TRAPPIST-1 was detected with an average count rate of 3 c ks^{-1}, approximately an order of magnitude lower than the average count rate found by Wheatley et al. (2017). Analysis of all available archival data suggested that the Wheatley et al. (2017) result was dominated by a strong flare(s), thus we take our observation to represent the "typical" or quiescent X-ray flux.

3. SED

For the most part, the SED was generated following the same procedure as for the MUSCLES SEDs as described by Loyd et al. (2016). Figure 1 shows the full SED and the wavelength ranges covered by the different observational and model sources. Factors unique to TRAPPIST-1 as well as departures from the MUSCLES techniques are described below. When discussing specific wavelength regions we follow the definitions used for the MUSCLES program by France et al. (2016): X-ray: 5–100 Å; EUV: 100–911 Å; FUV: 911–1700 Å; NUV: 1700–3200 Å and optical/NIR: 3200 Å–10.0 μm.

3.1. *X-ray*

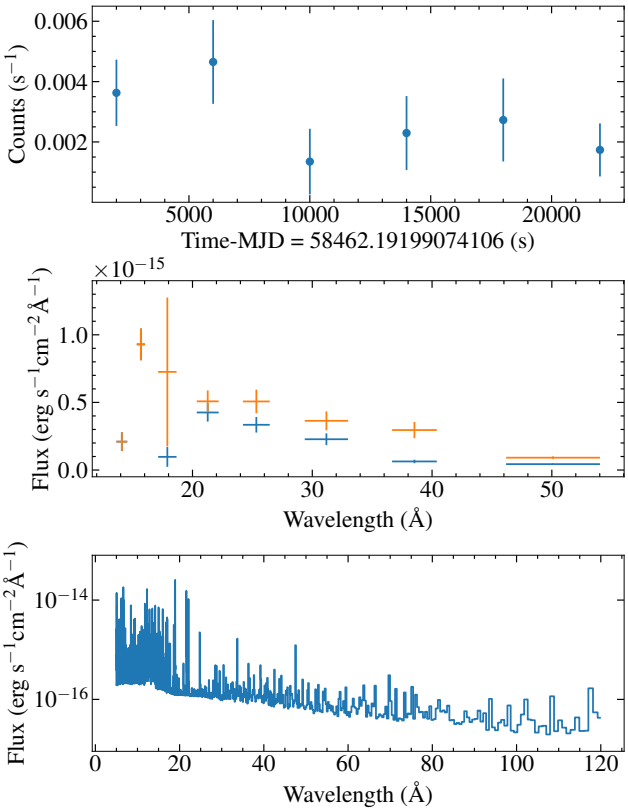

Figure 2. Top: X-ray lightcurve of TRAPPIST-1 observed on 2018 December 10. Middle: *XMM* spectrum of TRAPPIST-1. The extracted flux is shown in blue and the model-corrected flux in orange. Bottom: APEC model used to correct the TRAPPIST-1 spectrum and provide the 50–120 Å range of the SED.

The *XMM* spectrum was fit using the XSPEC package (Arnaud 1996) with models generated using the Astrophysical Plasma Emission Code (APEC, Smith et al. 2001). The data were best fit by a two-temperature model (kT = 0.2, 0.4) and a metallicity of 0.4 Solar. As detailed in Loyd et al. (2016), the model was then used to correct the data at lower energies for instrumental effects to produce the final X-ray spectrum used in the SED, covering the wavelength range of 14–50 Å. The integrated observed flux over the energy range 0.1-10 keV was 2×10^{-14} erg s^{-1} cm^{-2}. The APEC model extends beyond the wavelength range covered by the data to 120 Å and we include that extension in the final SED.

3.2. *Extreme-Ultraviolet and DEM modelling*

The most significant departure from the MUSCLES procedure is in the Extreme-Ultraviolet (EUV), where we have replaced the Linsky et al. (2014) empirical scaling relations with a Differential Emission Measurement (DEM) model, which estimates the chromospheric, transition region and coronal emission based on the strength of the detected lines in the FUV spectrum and the X-ray flux. A model spectrum is required as the region spanning 100–1100 Å is unobservable, both physically due to absorption from interstellar hydrogen between 400-900 Å, and a lack of currently operating instruments that can observe the ranges 100–400 Å and 900–1100 Å(*HST*/COS and *Chandra* do have some modes that extend down to 900 Å and up to 175 Å respectively, but these were not sensitive enough to be practical for this program). The DEM model is described in detail in Section 5.

3.3. *Far- and Near- Ultraviolet*

The H I 1215.67 Å Lyman α line is clearly visible in our coadded STIS G140M spectrum, but is heavily affected by both interstellar absorption and terrestrial airglow. We reconstructed the full Lyman α profile with a technique derived from Youngblood et al. (2016). In order to benefit from the increased S/N offered by spectra taken before the Mega-MUSCLES observation while simultaneously accounting for possible intrinsic stellar variability, we fit both

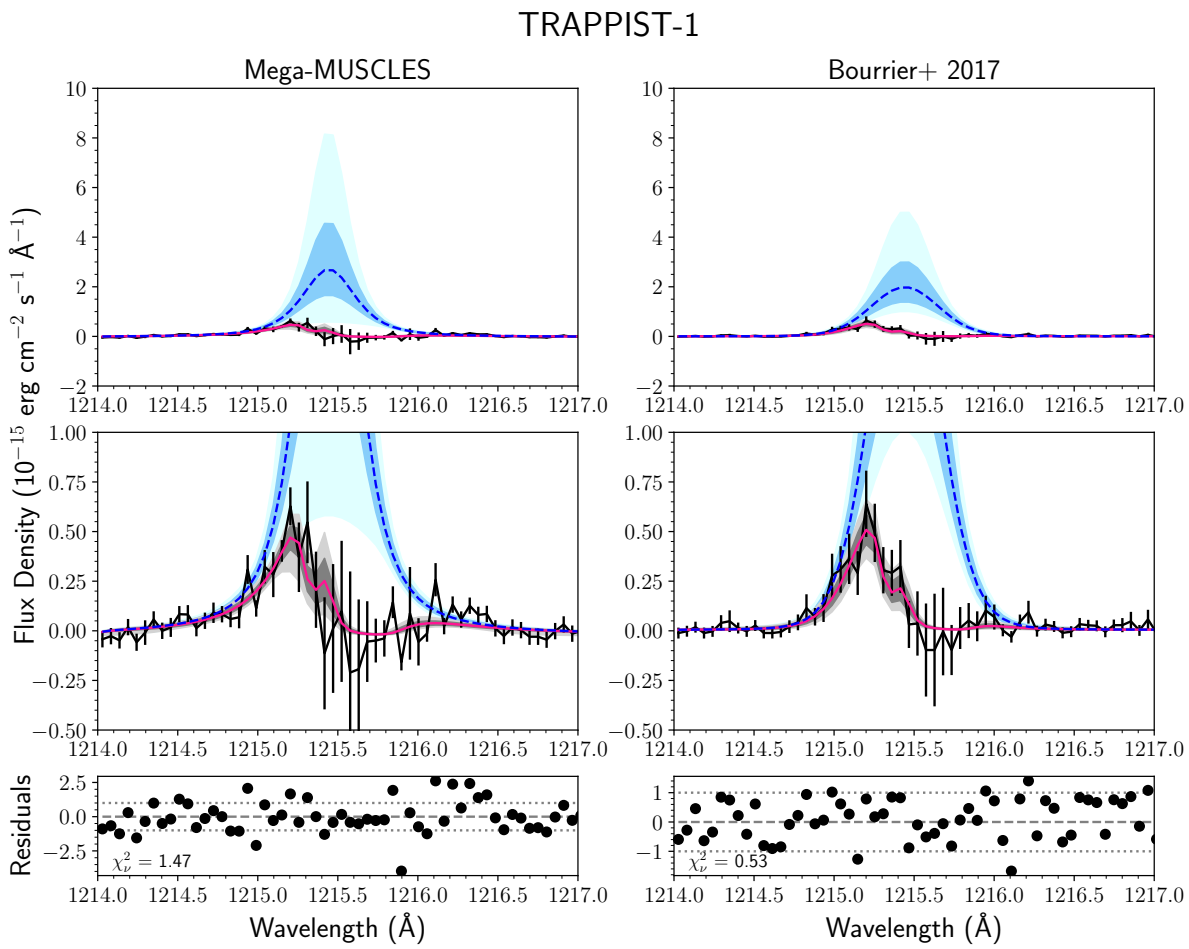

Figure 3. Best-fit models and intrinsic Lyman alpha profiles are shown from a simultaneous fit to the new spectrum presented in this work and the spectrum presented in Bourrier et al. (2017a). The ISM properties were forced to be the same for the two spectra, but the intrinsic emission profiles were allowed to vary, to account for either intrinsic stellar variability or differences in the flux calibration between the two datasets. The solid pink lines show the best fits to the data (black lines with error bars), with the dark and light shaded regions corresponding to the 68% and 95% confidence intervals, respectively. The dashed blue lines show the intrinsic emission profiles corresponding to the best fit models, and the dark blue and light blue shaded regions represent the 68% and 95% confidence intervals, respectively. The bottom panels show the residuals of the fit, or the best fit models subtracted from the data and divided by the data uncertainty. The reduced chi-squared values are printed in the same panels.

the new Mega-MUSCLES observation and the observation from Bourrier et al. (2017a) simultaneously. We use Voigt profiles for the stellar emission as well as for the ISM absorption, but require the ISM absorption to be the same for both observations. The velocity centroid for both Voigt emission profiles are given a Gaussian prior with mean -56.3±1 km s^{-1} (Reiners & Basri 2009a). We do not fix them to the same value to account for wavelength solution errors between the two observations, and we parameterize the velocity centroid of the ISM absorption as an offset from the stellar emission. Based on the measured stellar radial velocity and the predicted ISM radial velocity along TRAPPIST-1's sightline (-1.25±1.37 km s^{-1}, Redfield & Linsky 2008), we give the offset ISM velocity parameter a Gaussian prior with mean +55.05±1.70 km s^{-1}, adding the stellar radial velocity and ISM model uncertainties in quadrature. We fix the Doppler b value of the ISM absorption profile to 11.5 km s^{-1} and D/H= 1.5×10^{-5}, both standard values for the local ISM (Wood 2004). All other parameters were varied with uniform priors. Figure 3 shows the spectrum and reconstructed line profile. We report the median and the 68 per cent confidence interval as our best fit values and 1σ error bars. We found an integrated flux of $F_{\mathrm{Ly}\alpha} = (1.40^{+0.60}_{-0.36}) \times 10^{-14}$ erg s^{-1} cm^{-2} for the

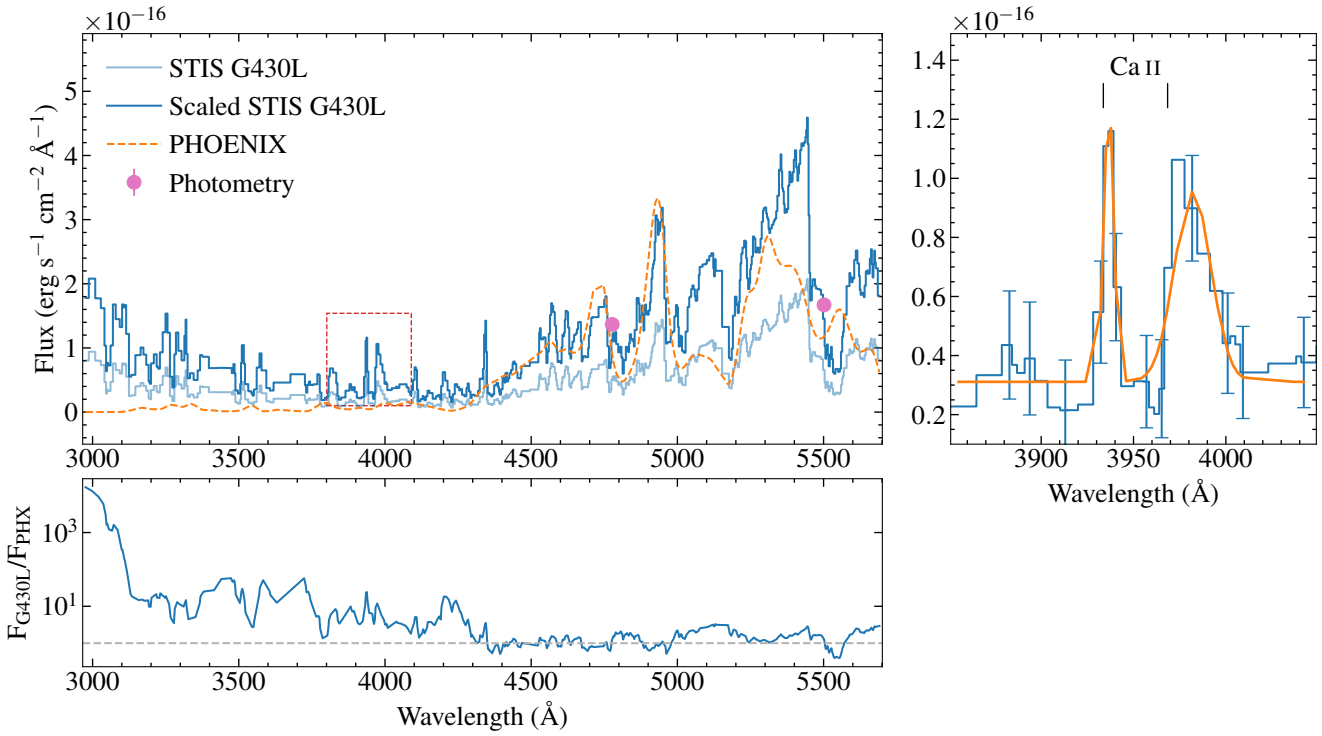

Figure 4. Top left: STIS G140L spectrum (blue) scaled to Pan-STARSS g and *Gaia* B_p photometry (Gonzales et al. 2019) and compared with the PHOENIX model (orange). The spectrum has been smoothed by a factor 2 for clarity, and the PHOENIX model been convolved to the resolution of the observed spectrum. Bottom left: The STIS spectrum is in good agreement with the PHOENIX model at longer wavelengths, but departs from it at shorter wavelengths as flux from the chromosphere begins to dominate. Right: Enlarged view of the region in the red box showing Ca II H&K emission lines, along with the Gaussian fits (orange) used to measure the emission line fluxes (Table 1).

Mega-MUSCLES observation, and $F_{\mathrm{Ly}\alpha} = (1.09^{+0.40}_{-0.27}) \times 10^{-14}\,\mathrm{erg\,s^{-1}\,cm^{-2}}$ for the Bourrier et al. (2017a) observation. This value is larger but within $1\,\sigma$ of the flux ($(8.18^{+1.64}_{-3.27}) \times 10^{-15}\,\mathrm{erg\,s^{-1}\,cm^{-2}}$) found by Bourrier et al. (2017a), and is explained by our fit's larger column density ($\log_{10}$ N(HI) = 18.4±0.1, compared to 18.3±0.2 from Bourrier et al. 2017a). However, these column densities and reconstructed fluxes are consistent with the result from Bourrier et al. 2017b within 1-sigma, and we do not detect any statistically significant intrinsic stellar variability between the two observations.

The COS FUV spectrum was contaminated by airglow from Lyman α and O I over the wavelength ranges 1214–1217 Å and 1301–1307 Å respectively. Both ranges were removed and replaced by the reconstructed Lyman α profile in the first case and by a polynomial fit to the spectrum on either side in the second. As we therefore have no information at these wavelengths, for the rest of this paper we assume that there is zero flux from O I at TRAPPIST-1.

The COS NUV observations covered the wavelength ranges 1700–2100 Å and 2800–3200 Å leaving a 700 Å gap. This gap is partially covered by a second order spectrum spanning 1950–2150 Å, but the signal was so weak that we chose not to include it. The gap was filled with a polynomial fit to the two wavelength regions, with the range 2790–2805 Å masked out to remove contributions from the Mg II 2800 Å lines.

3.4. *Optical to infrared*

3.4.1. *STIS G430L*

Figure 4 shows the STIS G430L spectrum of TRAPPIST-1 covering the waveband 2900–5700 AA. Comparison with the PHOENIX model and PanSTARSS g and *Gaia* B_p photometry collected by Gonzales et al. (2019) suggests that the spectrum is incorrectly flux calibrated, possibly due to imprecise slit centering during the observation. Synthetic g and B_p photometry was produced by integrating the spectrum over the appropriate passbands. The spectrum was scaled by the average of the ratios of the synthetic photometry to the measured photometry. The scaled spectrum

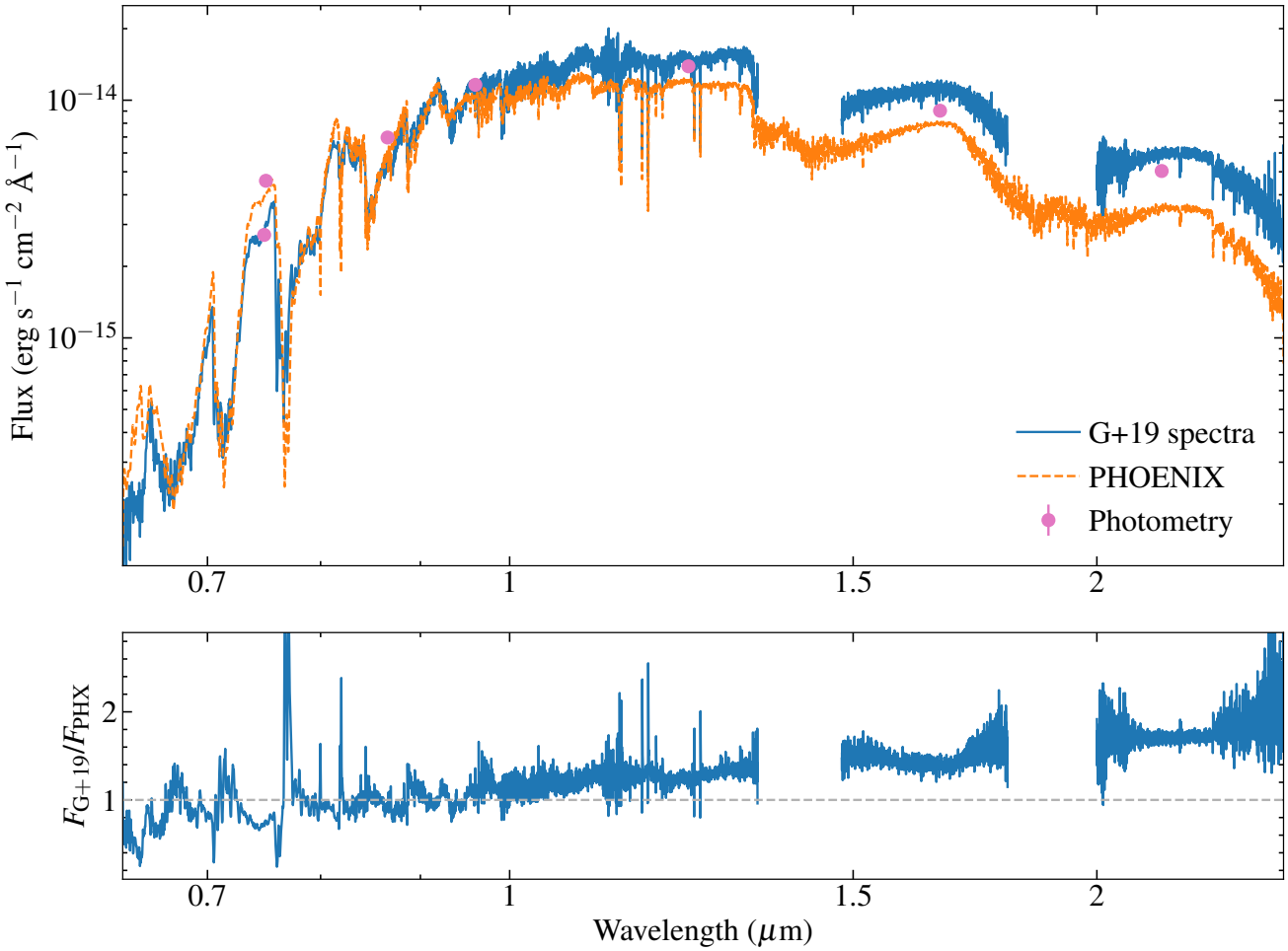

Figure 5. Top: PHOENIX model compared with the spectrum and photometry from Gonzales et al. (2019). The model spectrum has been convolved to the resolution of the observed spectrum. Bottom: The ratio of the model flux to the observed spectrum.

is in good agreement with the PHOENIX model at longer wavelengths, but diverges at wavelengths $\lesssim$4500 Å as flux from the chromosphere, which is not included in the model, begins to dominate the spectrum. The G430L spectrum contains features consistent with emission from the Ca II H&K lines at 3968.4673 and 3933.6614 Å. The Ca H line is blended with emission from the H *epsilon* line so is presented as an upper limit in Table 1.

3.4.2. *PHOENIX*

Wavelengths from 5700Å to 10 μm are filled with a PHOENIX photospheric model spectrum from the Lyon BT-Settl [DIR] CIFIST2011_2015 grid[1](Allard 2016; Baraffe et al. 2015) as no ground-based spectroscopy of TRAPPIST-1 contemporaneous with our *HST* and *XMM* observations are available. Gonzales et al. (2019) used distance-calibrated spectra and photometry to obtain atmospheric parameters of TRAPPIST-1 of $T_{\rm eff} = 2628 \pm 42$ K and $\log g = 5.21 \pm 0.06$ dex. We obtained the four closest moddels ($T_{\rm eff}, \log g$ = 2600, 5.0; 2700, 5.0; 2600, 5.5; 2700, 5.5) and linearly interpolated them onto the measured parameters using the SCIPY griddata routine. The model flux is then scaled by the square of the ratio of the measured radius and distance of TRAPPIST-1 ($1.16 \pm 0.03\,R_{\rm Jup}$ and 12.43 ± 0.02 pc respectively, Gonzales et al. 2019). The BT-Settl models extend to 1000 μm, but to avoid the SED file size becoming too large we truncated the model at 10 μm. The removed flux contributed less than one per cent of the total integrated

[1] https://phoenix.ens-lyon.fr/Grids/BT-Settl/

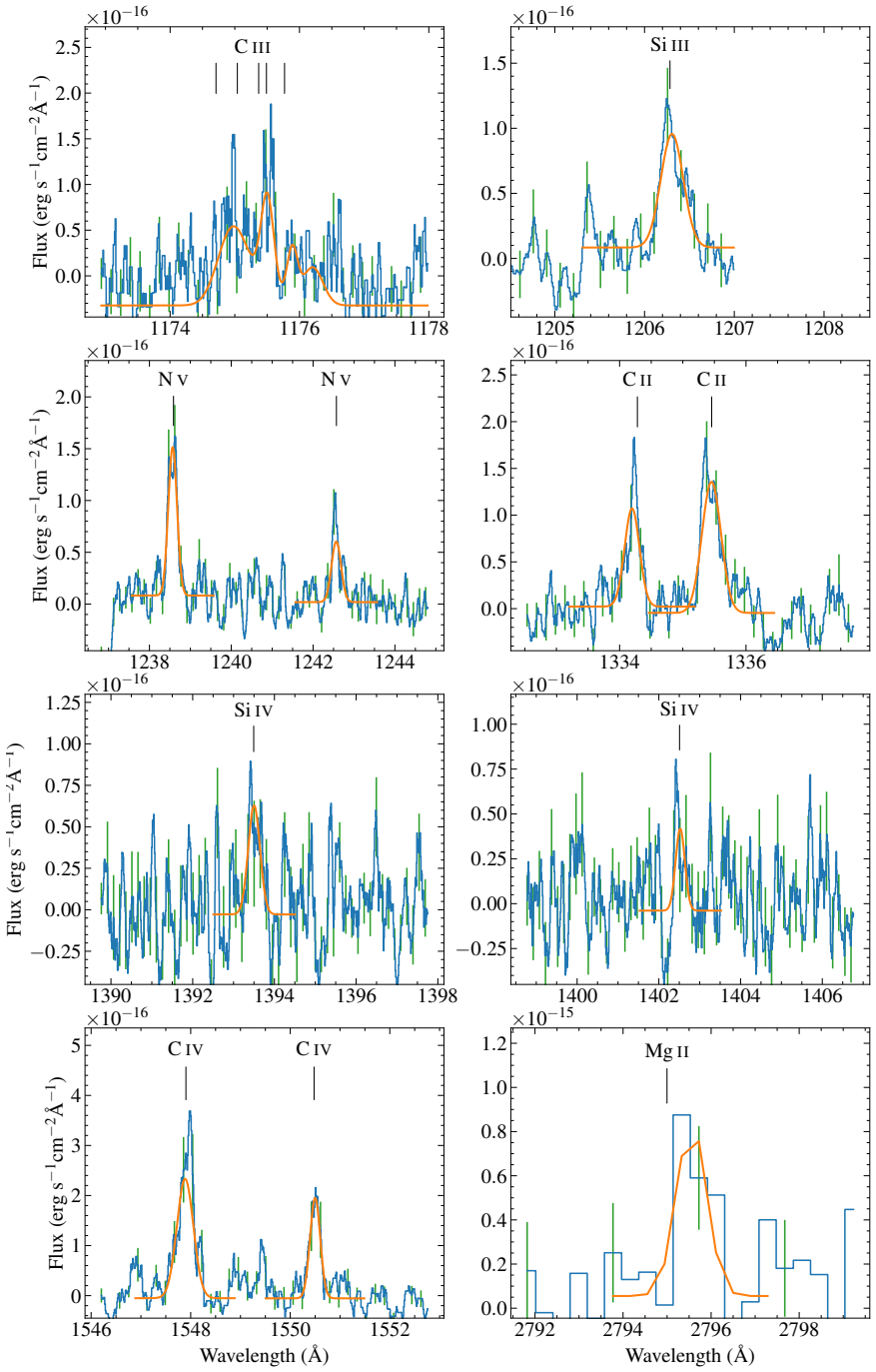

Figure 6. Detected emission lines in COS spectra of TRAPPIST-1 (blue) and the fit used to measure the integrated fluxes (orange). Example error bars on the flux values are shown in green. The data were smoothed with a 10-point boxcar for clarity, with the exception of the region around the Mg II lines. Line positions were taken from NIST and shifted by the $-56.3\,\mathrm{km\,s^{-1}}$ radial velocity of TRAPPIST-1 (Reiners & Basri 2009b).

flux of the model. Figure 5 compares the PHOENIX model with the data from Gonzales et al. (2019) used to measure the atmospheric parameters. The model appears to be offset from the data by a linear function, over-predicting the data at short wavelengths and underpredicting it a longer wavelengths.

4. EMISSION LINE FLUX MEASUREMENTS

Species	λ_{rest} (Å)	Flux (10^{-18} erg s^{-1} cm^{-2})
C III	1174.0	101 ± 27
Si III	1206.51	25.0 ± 6.3
N V	1238.821	36 ± 6.1
N V	1242.804	16 ± 10.0
Si II	1264.73	≤ 4.2
Si II	1298.95	4.4 ± 3.5
Si II	1309.28	5.7 ± 2.6
C II	1334.532	30 ± 20
C II	1335.708	55 ± 19
C I	1351.657	≤ 9.5
O I	1355.598	≤ 14
O V	1371.292	≤ 12
Fe II	1391.08	≤ 13
Si IV	1393.755	25 ± 19
C I	1401.156	≤ 7.5
Si IV	1402.77	14.0 ± 7.6
Si II	1526.71	≤ 7.3
Si II	1533.43	≤ 15
C IV	1548.195	100 ± 46
C IV	1550.77	53 ± 17
C I	1561.0	≤ 18
He II	1643.0	≤ 26
O III	1666.153	≤ 35
Al II	1670.787	≤ 45
Al I	1766.39	≤ 71
Mg II	2795.523	620 ± 29
Mg II	2802.697	≤ 340
Ca II	3933.6614	380 ± 100
Ca II	3968.4673	$\leq 780^{*}$

Table 1. Integrated fluxes for ultraviolet emission line lists compiled by Linsky (2017) and Peacock et al. (2019). Lines at wavelengths not covered by our observations were omitted. *Detected, but blended with H ϵ.

Producing the DEM and semi-empirical models discussed below required identifying and measuring the fluxes of emission lines in the COS spectra. We used the list of ultraviolet emission lines formed in stellar chromospheres and transition regions from Table 2 of Linsky (2017). Where lines from the list were detected, we fit them using a Gaussian profile combined with a linear fit to the surrounding continuum to account for incorrect background subtraction (Figure 6). The flux is given as the integral of the Gaussian adjusted by the y-value of the linear fit, along with the propagated statistical error of the fit. Where lines where not detected we measured an upper limit as the integral of a section of flux with width equal to twice the average FWHM of the fitted lines in that spectrum. An exception is the C III 1176 Å multiplet, where due to the complexity of the line profile the flux was measured as the integral of the flux between 1774.5–1776.5Å with the uncertainty estimated as the sum of the RMS of two adjacent 1 Å wide regions. We also measured any lines from Table 5 of Peacock et al. (2019) not featured in the Linsky (2017) line list in order to compare the observed and predicted fluxes (Section 7).

5. DIFFERENTIAL EMISSION MEASURE

The differential emission measure (DEM) describes the amount of emitting plasma as a function of temperature for an optically thin plasma in coronal equilibrium (Warren et al. 1998; Louden et al. 2017), allowing us to predict the fluxes of emission lines formed in the coronal atmosphere if we have a functional form to describe the DEM. The DEM combined with the emissivity of a particular emission line determines the emission flux in that line emitted by a star. By measuring the flux of FUV emission lines formed at $\sim 10^5$ K and the X-ray flux formed at $\gtrsim 10^6$ K, we can

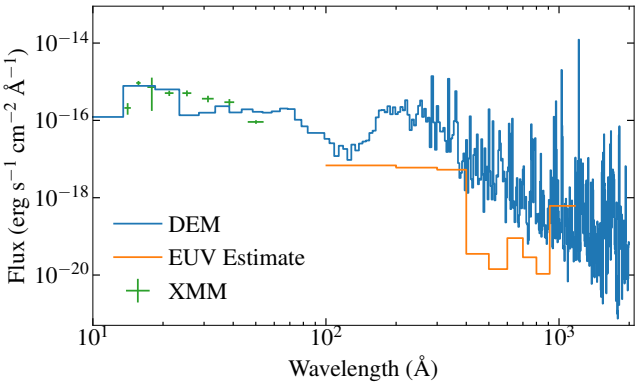

Figure 7. Comparison of the DEM model with the EUV/Lyman α relationships of Linsky et al. (2014), and the *XMM* spectrum.

constrain the DEM by assuming it is well-described by a smooth low-order polynomial across the temperature range relevant to the chromosphere, transition region, and corona. This operates under the same principle as the Linsky et al. (2014) empirical scaling relations, but is tailored more specifically to the star by using more lines to resolve the structure of the star's upper atmosphere at a finer temperature resolution. Combining the differential emission measure with atomic data from `CHIANTI v8.0` (Dere et al. 1997; Del Zanna et al. 2015), we estimate the EUV spectrum of TRAPPIST-1 between 10 to 912 Å, incorporating the errors in fitting the differential emission measure forward to the predicted EUV spectrum. Our implementation is similar to the method employed by Louden et al. (2017); details of the Mega-MUSCLES DEM prescription will be described in a future paper (Duvvuri et al. in prep).

6. SEMI-EMPIRICAL MODEL

Given the unavoidable low signal-to-noise of ultraviolet observations of late M-dwarfs in general and TRAPPIST-1 in particular, the Mega-MUSCLES data products will also include semi-empirical models constructed from the observed spectra, which we recommend as inputs for model planetary atmosphere studies as they avoid potentially biasing the models with the large amount of noise in the observed spectra. The semi-empirical model for TRAPPIST-1 is shown in Figure 8. Four models are used, including the APEC, DEM and PHOENIX models already discussed. The fourth model replaces the *HST* spectra covering 1100–4200 Å. The model is constructed by first fitting a polynomial to the DEM model and the blue end ($\lambda < 4200$) of the STIS G430L spectrum to create a baseline flux. Note that this does not represent just the chromospheric/coronal continuum emission, but rather the combination of a forest of weak emission lines plus any continuum emission in that wavelength range. We then added the reconstructed Lyman α line and the fits to the emission lines shown in Figure 6, as well as the PHOENIX spectrum at those wavelengths, to produce the final spectrum section.

Figure 8 compares our final semi-empirical model SED with the quiet Solar spectrum (Woods et al. 2009). The Solar spectrum has been moved to the distance of TRAPPIST-1 and scaled by the ratio of the blackbody luminosities of the photospheres of the two stars, such that the photospheric flux for each spectrum is the same as the irradiation Earth receives. The comparison clearly demonstrates the relative difference in high-energy flux between TRAPPIST-1 and the Sun, implying that any planet receiving the same photospheric flux from TRAPPIST-1 as (for example) the Earth receives from the Sun, is experiencing high-energy flux levels that are several orders of magnitude higher (Figure 9, even when the star is not flaring.

7. COMPARISON WITH MODEL SPECTRA

Peacock et al. (2019) extended the PHOENIX stellar atmosphere code into the ultraviolet by adding chromosphere and transition region , providing model SEDs of the TRAPPIST-1 chromosphere against which we can compare our observations. The three PHOENIX models were calibrated to the Bourrier et al. (2017a) Lyman α flux (1A) and distance-adjusted GALEX photometry of stars with similar spectral types (models 2A and 2B).

Figure 10 compares the predicted line strengths given in Table 5 of Peacock et al. (2019) with the line fluxes measured from our COS data (Table 1) as a function of formation temperature and wavelength. For all three models, the agreement between the predicted and measured line fluxes is in general poor. The Lyman α-scaled model 1A

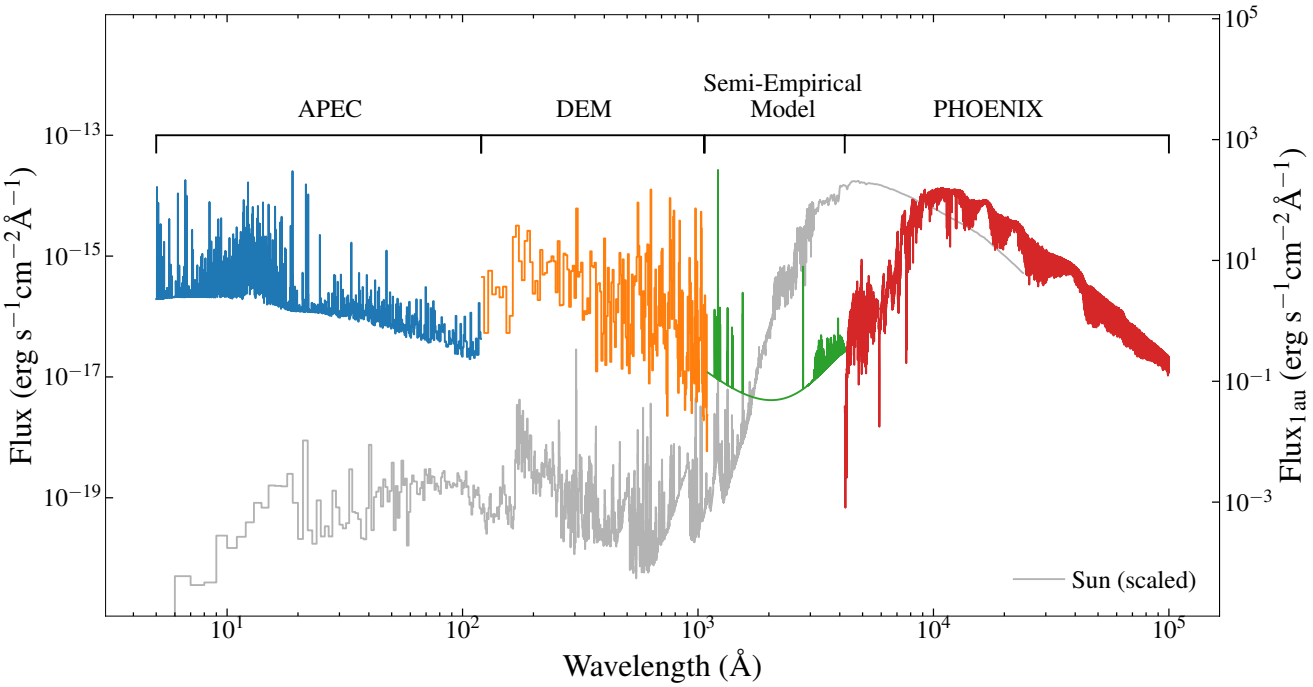

Figure 8. Semi-empirical model spectrum of Trappist-1. The four different models components used are labeled above the spectrum, and the PHOENIX model has been rebinned to 1 Å for clarity. The spectrum is compared with the quiet Solar spectrum Woods et al. (2009), scaled to have the same blackbody photospheric flux as TRAPPIST-1. The left axis shows the flux received from Trappist-1 at Earth, whereas the right shows the flux received at at the 1 au equivalent distance, i.e. the spectrum of Trappist-1 at a distance receiving the same photospheric flux as at 1 au from the Sun

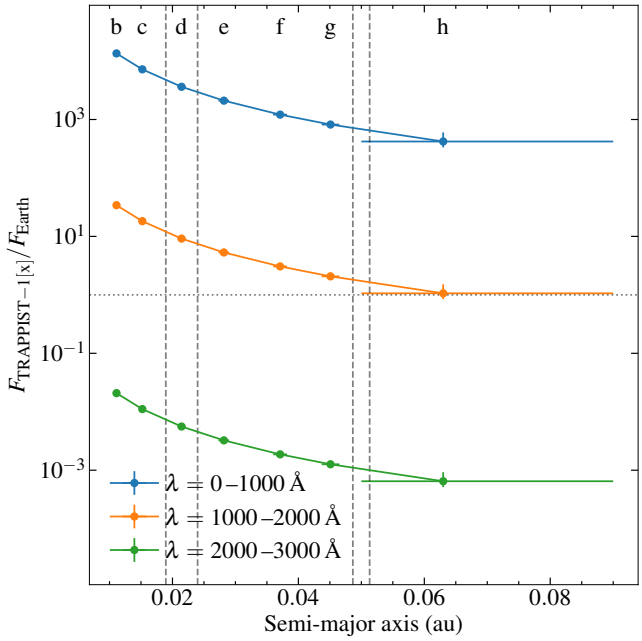

Figure 9. Fluxes at different wavebands experienced by the TRAPPIST-1 planets compared with the Earth. The dashed lines show empirical (including TRAPPIST-1 d) and conservative (excluding TRAPPIST-1 d) edges of the temperate zone for 1 $M_\oplus$ planets as modelled by Kopparapu et al. (2014).

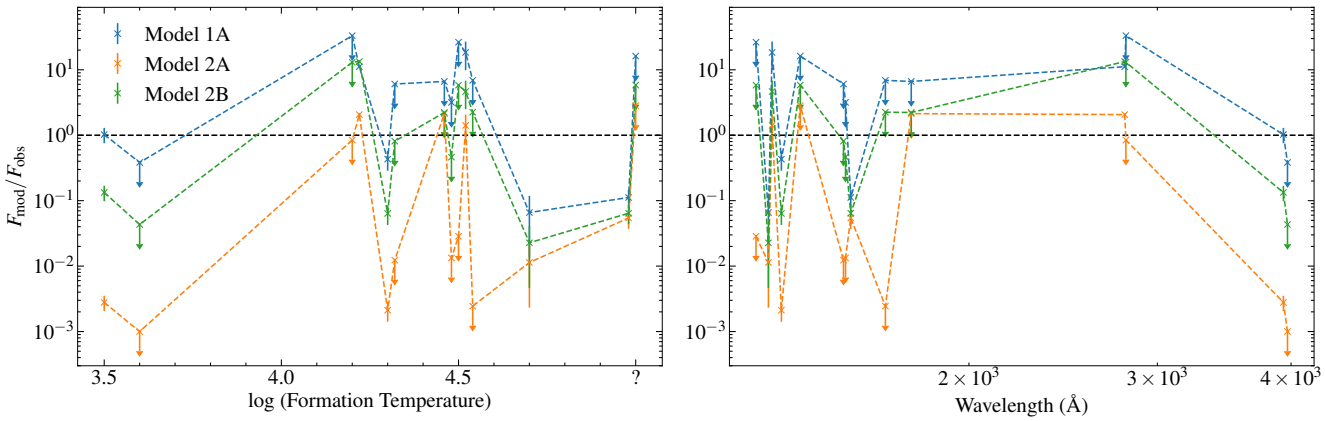

Figure 10. Comparison of the integrated flux of detected emission lines with predicted fluxes given in Table 5 of Peacock et al. (2019) as function of formation temperature (left) and wavelength (right). We were unable to find a measured formation temperature for Fe II 1391 Å.

accurately predicts the measured fluxes of the C II and Ca II lines, but predicts multiple lines at values ~ 10 times higher than the upper limits placed on their fluxes here. No trend between the accuracy of the predicted fluxes and either formation temperature or wavelength.

8. HIGH-LEVEL SCIENCE PRODUCTS

The TRAPPIST-1 SED will be made available at or before publication of this paper on the MUSCLES Treasury Survey Page at the Mikulski Archive for Space Telescopes (MAST): https://archive.stsci.edu/prepds/muscles/. Available products will include the standard data products provided by the MUSCLES survey (i.e., the SED at native and 1 Å resolutions along with the component observations and models), along with the new Semi-empirical model SED at native and 1 Å resolutions. The remainder of the Mega-MUSCLES targets, listed at http://cos.colorado.edu/~kevinf/muscles.html, will be added to the database in the coming months. Users with an interest in any particular target can contact the first author for an expedited production of that SED.

9. CONCLUSION

We have constructed a panchromatic SED of the M8 star TRAPPIST-1, the first data product from the Mega-MUSCLES survey.

TRAPPIST-1 is the faintest target in the Mega-MUSCLES survey, and the SED presented here both represents the state-of-the-art for observation of the high-energy flux of low-mass stars and demonstrates the limits of our current observing facilities. Obtaining the ultraviolet spectroscopy pushed the capabilities of COS to their limits, with many expected emission lines remaining below the noise limit. The EUV spectrum cannot be observed with any currently operating facility. Improving on these observations, which is desirable given the continued importance of low-mass stars for exoplanet science, will require the launch of large-aperture space telescopes with ultraviolet capabilities and a dedicated EUV observatory (Youngblood et al. 2019).

We thank S. Peacock for providing the PHOENIX EUV models and E. Gonzales for providing the optical spectra and photometry. Based on observations made with the NASA/ESA Hubble Space Telescope, obtained from the Data Archive at the Space Telescope Science Institute, which is operated by the Association of Universities for Research in Astronomy, Inc., under NASA contract NAS 5-26555. These observations are associated with program # 15071. Support for program #15071 was provided by NASA through a grant from the Space Telescope Science Institute, which is operated by the Association of Universities for Research in Astronomy, Inc., under NASA contract NAS 5-26555. All of the *HST* data presented in this paper were obtained from the Mikulski Archive for Space Telescopes (MAST). AY acknowledges support by an appointment to the NASA Postdoctoral Program at Goddard Space Flight Center, administered by USRA through a contract with NASA. PCS acknowledges support by DLR under grant 50 OR 1901.

Facilities: *HST* (STIS and COS), *XMM-Newton*

Software: astropy (Astropy Collaboration, 2013), stistools, scipy

APPENDIX

REFERENCES

Airapetian, V. S., Glocer, A., Khazanov, G. V., et al. 2017, ApJL, 836, L3

Allard, F. 2016, in SF2A-2016: Proceedings of the Annual meeting of the French Society of Astronomy and Astrophysics, ed. C. Reylé, J. Richard, L. Cambrésy, M. Deleuil, E. Pécontal, L. Tresse, & I. Vauglin, 223–227

Arnaud, K. A. 1996, in Astronomical Society of the Pacific Conference Series, Vol. 101, Astronomical Data Analysis Software and Systems V, ed. G. H. Jacoby & J. Barnes, 17

Astropy Collaboration, Robitaille, T. P., Tollerud, E. J., et al. 2013, A&A, 558, A33

Baraffe, I., Homeier, D., Allard, F., & Chabrier, G. 2015, A&A, 577, A42

Barstow, J. K., & Irwin, P. G. J. 2016, MNRAS, 461, L92

Bourrier, V., Ehrenreich, D., Wheatley, P. J., et al. 2017a, A&A, 599, L3

Bourrier, V., de Wit, J., Bolmont, E., et al. 2017b, AJ, 154, 121

Burgasser, A. J., & Mamajek, E. E. 2017, ApJ, 845, 110

de Wit, J., Wakeford, H. R., Gillon, M., et al. 2016, Nature, 537, 69

Del Zanna, G., Dere, K. P., Young, P. R., Landi, E., & Mason, H. E. 2015, A&A, 582, A56

Dere, K. P., Landi, E., Mason, H. E., Monsignori Fossi, B. C., & Young, P. R. 1997, A&AS, 125, 149

France, K., Loyd, R. O. P., Youngblood, A., et al. 2016, ApJ, 820, 89

Gillon, M., Jehin, E., Lederer, S. M., et al. 2016, Nature, 533, 221

Gillon, M., Triaud, A. H. M. J., Demory, B.-O., et al. 2017, Nature, 542, 456

Gonzales, E. C., Faherty, J. K., Gagné, J., et al. 2019, arXiv e-prints, arXiv:1909.13859

Green, J. C., Froning, C. S., Osterman, S., et al. 2012, 744, 60

Kopparapu, R. K., Ramirez, R. M., SchottelKotte, J., et al. 2014, ApJL, 787, L29

Linsky, J. L. 2017, ARA&A, 55, 159

Linsky, J. L., Fontenla, J., & France, K. 2014, ApJ, 780, 61

Louden, T., Wheatley, P. J., & Briggs, K. 2017, MNRAS, 464, 2396

Loyd, R. O. P., France, K., Youngblood, A., et al. 2016, ApJ, 824, 102

Luger, R., Sestovic, M., Kruse, E., et al. 2017, Nature Astronomy, 1, 0129

Miguel, Y., Kaltenegger, L., Linsky, J. L., & Rugheimer, S. 2015, MNRAS, 446, 345

Morley, C. V., Kreidberg, L., Rustamkulov, Z., Robinson, T., & Fortney, J. J. 2017, ApJ, 850, 121

O'Malley-James, J. T., & Kaltenegger, L. 2017, MNRAS, 469, L26

Peacock, S., Barman, T., Shkolnik, E. L., Hauschildt, P. H., & Baron, E. 2019, ApJ, 871, 235

Redfield, S., & Linsky, J. L. 2008, ApJ, 673, 283

Reiners, A., & Basri, G. 2009a, ApJ, 705, 1416

—. 2009b, 496, 787

Ribas, I., Bolmont, E., Selsis, F., et al. 2016, A&A, 596, A111

Roettenbacher, R. M., & Kane, S. R. 2017, ApJ, 851, 77

Rugheimer, S., Segura, A., Kaltenegger, L., & Sasselov, D. 2015, ApJ, 806, 137

Smith, R. K., Brickhouse, N. S., Liedahl, D. A., & Raymond, J. C. 2001, ApJ, 556, L91

Veras, D., Armstrong, D. J., Blake, J. A., et al. 2018, Astrobiology, 18, 1106

Vida, K., Kővári, Z., Pál, A., Oláh, K., & Kriskovics, L. 2017, ApJ, 841, 124

Wang, S., Wu, D.-H., Barclay, T., & Laughlin, G. P. 2017, arXiv e-prints, arXiv:1704.04290

Warren, H. P., Mariska, J. T., & Lean, J. 1998, J. Geophys. Res., 103, 12077

Wheatley, P. J., Louden, T., Bourrier, V., Ehrenreich, D., & Gillon, M. 2017, MNRAS, 465, L74

Wood, B. E. 2004, Living Reviews in Solar Physics, 1, 2

Woodgate, B. E., Kimble, R. A., Bowers, C. W., et al. 1998, PASP, 110, 1183

Woods, T. N., Chamberlin, P. C., Harder, J. W., et al. 2009, Geophys. Res. Lett., 36, L01101

Youngblood, A., France, K., Loyd, R. O. P., et al. 2016, ApJ, 824, 101

Youngblood, A., Drake, J., Mason, J., et al. 2019, BAAS, 51, 300